ADVANCED MATERIALS
www.advmat.de

Bi-Interlayer Strategy for Modulating NiCoP-Based Heterostructure toward High-Performance Aqueous Energy Storage Devices

Jian Xu, Xiliang Gong, Zeshuo Meng, Peiyuan Chen, Haoshan Nan, Yaxin Li, Ting Deng, Dong Wang, Yi Zeng, Xiaoying Hu, Hongwei Tian, Zhiqiang Niu, and Weitao Zheng**

Nickel-cobalt (NiCo) phosphides (NCPs) possess high electrochemical activity, which makes them promising candidates for electrode materials in aqueous energy storage devices, such as supercapacitors and zinc (Zn) batteries. However, the actual specific capacitance and rate capability of NCPs require further improvement, which can be achieved through reasonable heterostructural design and loading conditions of active materials on substrates. Herein, novel hierarchical Bi-NCP heterogeneous structures with built-in electric fields consisting of bismuth (Bi) interlayers (electrodeposited on carbon cloth (CC)) are designed and fabricated to ensure the formation of uniform high-load layered active materials for efficient charge and ion transport. The resulting CC/Bi-NCP electrodes show a uniform, continuous, and high mass loading (>3.5 mg) with a superior capacitance reaching 1200 F g^{-1} at 1 A g^{-1} and 4129 mF cm^{-2} at 1 mA cm^{-2} combined with high-rate capability and durable cyclic stability. Moreover, assembled hybrid supercapacitors (HSCs), supercapatteries, and alkaline Zn-ion (AZBs) batteries constructed using these electrodes deliver high energy densities of 64.4, 81.8, and 319.1 Wh kg^{-1}, respectively. Overall, the constructed NCPs with excellent aqueous energy storage performance have the potential for the development of novel transition metal-based heterostructure electrodes for advanced energy devices.

1. Introduction

The surge of intelligent telecommunication, transportation, and wearable devices in modern society requires the development of efficient energy storage technologies.[1] Among power devices, supercapacitors provide high power densities, rapid charge/discharge rates, and long service life. However, their low energy densities hinder practical applications in various fields.[2] Hybrid supercapacitors (HSCs) and supercapacitor batteries offer promising application prospects due to integrated electrodes with distinct energy storage mechanisms, resulting in high power and extended cycle life of capacitors combined with elevated energy characteristics of batteries.[3] Another type of energy device includes alkaline Zn-ion batteries (AZBs), which have attracted increasing attention due to their high theoretical capacity (820 mAh g^{-1}), more negative electrode potential (−1.26 V vs SHE), environmental friendliness, and low cost of Zn metal

J. Xu, X. Gong, Z. Meng, H. Nan, Y. Li, T. Deng, D. Wang, Y. Zeng, H. Tian, W. Zheng
Key Laboratory of Automobile Materials MOE
School of Materials & Engineering
Jilin Provincial International Cooperation Key Laboratory of High-Efficiency Clean Energy Materials
Jilin University
Changchun 130012, China
E-mail: tianhw@jlu.edu.cn; wtzheng@jlu.edu.cn

X. Gong
Department of Chemistry and Biochemistry
University of Maryland
College Park, MD 20742, USA

P. Chen
College of Physics
Jilin University
Changchun 130012, China

X. Hu
College of Science and Laboratory of Materials Design and Quantum Simulation
Changchun University
Changchun 130022, China

Z. Niu
Key Laboratory of Advanced Energy Materials Chemistry (Ministry of Education)
Nankai University
Tianjin 300071, China

The ORCID identification number(s) for the author(s) of this article can be found under https://doi.org/10.1002/adma.202401452

DOI: 10.1002/adma.202401452

anode.[4] For both HSCs and AZBs, the development of electrode materials with high specific capacity, elevated rate capability, and long-lasting cycle stability is the key to realizing efficient aqueous storage.

Nickel-cobalt (NiCo) transition metal phosphides (TMPs) are characterized by abundant redox reactions, which endow them with outstanding theoretical capacity.[5] Besides, the weaker M-P bonds than M-O bonds provide more active sites for the occurrence of electrochemical conversion processes. Notably, electrons are not strictly confined around phosphorus atoms; therefore, strong M-M interactions still exist to allow for rapid electron transport caused by strong electron delocalization in the sublattice. Consequently, TMPs often show higher conductivity and quasi-metallic properties.[6] However, the thermodynamic stability of TMPs is lower than those of corresponding oxides or even sulfides under aqueous electrochemical conditions, which may result in surface passivation of TMPs during electrochemical energy storage. This, in turn, may lead to uneven electric fields at the electrode/electrolyte interface, thereby reducing electrode conductivity and surface charge transfer kinetics. Therefore, the actual electrochemical performance of TMPs is not ideal and requires further improvement.

Heterostructure engineering can be effectively used to improve the electrochemical performance of NiCo-based TMPs. Most intuitively, combining selected TMPs with other materials may inherit the advantages of each part to improve the composite performance. From the morphological standpoint of electrode materials, the formation of heterogeneous structures may enhance the overall porosity, form more dispersed microstructures, and generate three-dimensional (3D) interconnected structures with inhibited agglomeration, conducive to increased specific surface area and formation of rich redox active sites.[7] Moreover, the construction of heterostructures can create defects and vacancies, conducive to regulating the electron/ion transfer efficiency.[8] From the perspective of electronic structure of electrode materials, the heterostructure can change the local charge distribution and form an internal electric field, affecting the electrochemical performance of electrodes. For instance, Bai et al. improved the life and safety of Zinc (Zn)-ion batteries by constructing a hierarchical heterostructure with induced ferroelectric polarization and internal electric fields, suitable for improving the chaotic ion diffusion path caused by uneven local electrolyte concentration.[4] Li et al. synthesized in situ dissociated heterostructures with P-type reverse barrier layers, suitable for effective customization electronic structure, and established internal potential around the heterojunction for improved OH^- adsorption and electron/ion conductivity.[9] Hussain et al. enhanced the surface dynamics of electrodes through the formation of heterogeneous structures due to the induced internal electric field at the heterogeneous interface.[10] However, the difference between electrons and lattice at the heterogeneous interface of unsuitable heterostructures can also reduce ion and electron transfer kinetics.[11] Therefore, enhancement in the electron and ion transfer kinetics of NiCo phosphide (NCP) by selecting appropriate composite materials and designing suitable heterostructures is highly desirable for advanced applications.

Besides, the electrochemical performance of NiCo-based TMPs can be enhanced through direct loading onto conductive substrates to form integrated electrodes with alleviated aggregation of electrode materials and enhanced conductivity with more reaction sites, thereby improving electrochemical performance. These integrated electrodes can be constructed through electrodeposition, advantageous in terms of cost-effectiveness, high efficiency, mild reaction conditions, and highly controllable reaction process.[12] The uniform electrodeposition of active substances on electrodes is crucial for the migration of electrolyte ions to the electrode and the resulting electrochemical reaction kinetics.[13] On the other hand, mass loading is vital for the overall capacity and energy of constructed devices. Furthermore, the substrate on which the material is electrodeposited may also impact the uniformity and mass loading of the material. Carbon cloth (CC) with good conductivity, lightweight, and superior foldability has widely been used as a substrate for integrated electrodes. However, electrodeposition of layers with good uniformity and high-mass loading is difficult due to its hydrophobicity.[14] E.g., our previously constructed $NiCo_2O_4$ on CC showed low mass loading and discontinuous distribution.[15] Thus, to date, numerous strategies have been employed to improve the load and uniformity of electrodeposited layers, particularly linked to plating conditions (temperature changes and introduction of external fields),[16] optimization of substrate surface states (strong acid treatment),[17] and electrolyte formulation (addition of surfactants and additives).[18] However, the use of organic reagents, strong acids, heat sources, or magnetic fields is disadvantageous due to their environmental contamination, safety issues, requirement for highly trained professionals, and so on. In contrast, a layer of metal or metal compounds (interlayer) can be constructed on the CC surface through simple methods. The resulting interlayer can change the surface state of the CC, thereby modulating the electrodeposition kinetics of the transition metal oxide/hydroxide active materials (outer layer) for high-mass loading, continuous, and uniform integrated electrodes.

Among these active materials, bismuth (Bi) can be utilized as a suitable interlayer material owing to its abundant reserves, low toxicity, and suitable layered structure with large internal space and easy phase transformation.[19] These features make Bi a potential candidate for customization and designability. Previous catalytic studies have shown Bi acting as an electron donor for heterostructures due to its high Fermi level position, is suitable for the promoted flow of charge carriers at heterogeneous interfaces.[20] For energy storage, numerous studies have shown that the introduction of Bi into composite materials could introduce new electronic states for increased electronic conductivity and enhanced structural stability.[21] For instance, Wang et al. introduced Bi metal into ZnO electrode to reduce the nucleation barrier of Zn, adjust the plating/stripping behavior of Zn, and guide its uniform deposition.[22] Accordingly, Bi can be employed to construct interlayers, which can regulate the electrodeposition process and form heterostructures with NCP and adjusted electronic structures for enhanced electrochemical performance of electrode materials.

Herein, a novel Bi interlayer with a dual role was constructed on CC by electrodeposition technique. The prepared Bi-interlayer improved the deposition kinetics of subsequent electrodeposition of Ni-Co hydroxide precursor, ensuring uniformity,

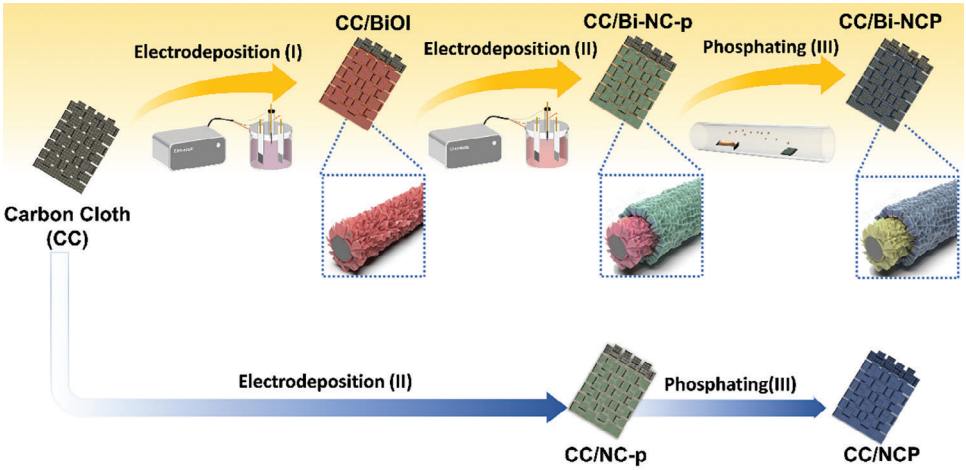

Scheme 1. Preparation process of CC/Bi-NCP and CC/NCP.

continuity, and high load quality. A hierarchical heterostructured CC/Bi-NCP electrode was then obtained by the simple phosphating process to control electron migration and electrode surface dynamics by adjusting the charge distribution at the heterogeneous interface. This provided more reactive sites, ensuring high specific capacitance and rate capability of electrodes. Furthermore, CC/Bi-NCP electrodes were used to assemble HSCs and AZBs, which exhibited excellent electrochemical performance. Overall, the developed dual-role interlayer strategy considered both the effects of the interlayer on the outer layer preparation process and the electrochemical performance of the heterostructure. Such design ideas could help the future development of hierarchical/composite electrodes for advanced electrochemical energy storage.

2. Results and Discussion

The preparation process of the CC/Bi-NCP heterostructure electrode is presented in **Scheme 1**. First, BiOI nanosheet arrays were plated on CC by electrodeposition to provide an effective adsorption layer and growth site for the subsequent electrodeposition of NiCo-hydroxide nanosheet arrays. Next, NiCo-hydroxide precursor was electrodeposited on CC/BiOI, during which BiOI underwent conversion into metallic Bi. The presence of Bi interlayer ensured uniform and high mass loading of NiCo-hydroxide precursor (NC-p). Finally, NaH_2PO_2 and CC/Bi-NiCo precursors (CC/Bi-NC-p) were annealed in a tubular furnace to obtain CC/Bi-NCP electrode. A series of CC/Bi-NCP-x (x = 1, 2, and 3) samples was then obtained at constant electrodeposition of NiCo-hydroxide precursor and variable electrodeposition time of BiOI. To emphasize the impact of Bi interlayer on the synthesis process and electrode performance, CC/NCP samples were obtained by electrodeposition of NiCo hydroxide precursor nanosheet arrays (NAs) on CC followed by phosphating. The universality of the Bi interlayer strategy was verified by conducting a set of Ni-Co oxide (NCO) experiments. The obtained samples were CC/Bi-Ni-Co oxide (CC/Bi-NCO) with a Bi interlayer and CC/Ni-Co oxide (CC/NCO) without a Bi interlayer.

2.1. Effect of BiOI Layer on Subsequent Electrodeposition Process

The influence of Bi-interlayer on the electrodeposition process of subsequent NC-p was investigated by characterizing the surface states of CC/BiOI and the original CC. Furthermore, the electrochemical behavior of NiCo hydroxide during electrodeposition, as well as the changes in surface components before and after NiCo hydroxide deposition were also analyzed. **Figures 1**a,b and S1 (Supporting Information) display that BiOI nanosheets obtained by electrodeposition uniformly covered the CC fibers in vertically arranged nanosheet arrays (Figure S2, Supporting Information). Compared to CC (Figure 1c), the contact angle of the CC/BiOI (Figure 1d) surface appeared to be significantly smaller, indicating better wettability that could be conducive to the rapid diffusion of electrolyte ions. After the deposition of BiOI NAs (Figure 1e), the Zeta potential of CC/BiOI surface changed from the original positive value (14.5 mV) of CC to a negative value (−7.7 mV), indicating better adsorption of metal cations (Co^{2+} and Ni^{2+}) by CC/BiOI.

For comparative analysis of the diffusion of metal cations in the electrolyte, both CC and CC/BiOI subjected to electrodeposition of NiCo hydroxide were analyzed by electrochemical impedance spectroscopy (EIS). Compared to CC (Figure 1f), the quasi-line in the low-frequency region of CC/BiOI showed an increased slope, indicating improved ion transport. After fitting (the equiv. circuit diagram is shown in Figure 1f inset), series resistance (Rs), transfer resistance (Rct), and Warburg impedance (Rw) of CC and CC/BiOI were obtained, and the specific values are listed in Table S1 (Supporting Information). Compared with CC, the intrinsic resistance of the CC/BiOI electrode gets slightly increased due to the introduction of BiOI species, which leads to a slight increase in the value of Rs. The Rct values of the CC/BiOI samples were significantly smaller, possibly due to the easy access of the ions into the interconnected BiOI nanosheets of the sample.[23] The obvious decrease of Rw indicates that the BiOI layer on CC shows a positive effect on the diffusion conditions of subsequent electrodeposition.[24] The diffusion resistance (Warburg factor, σ) of each sample was derived from the

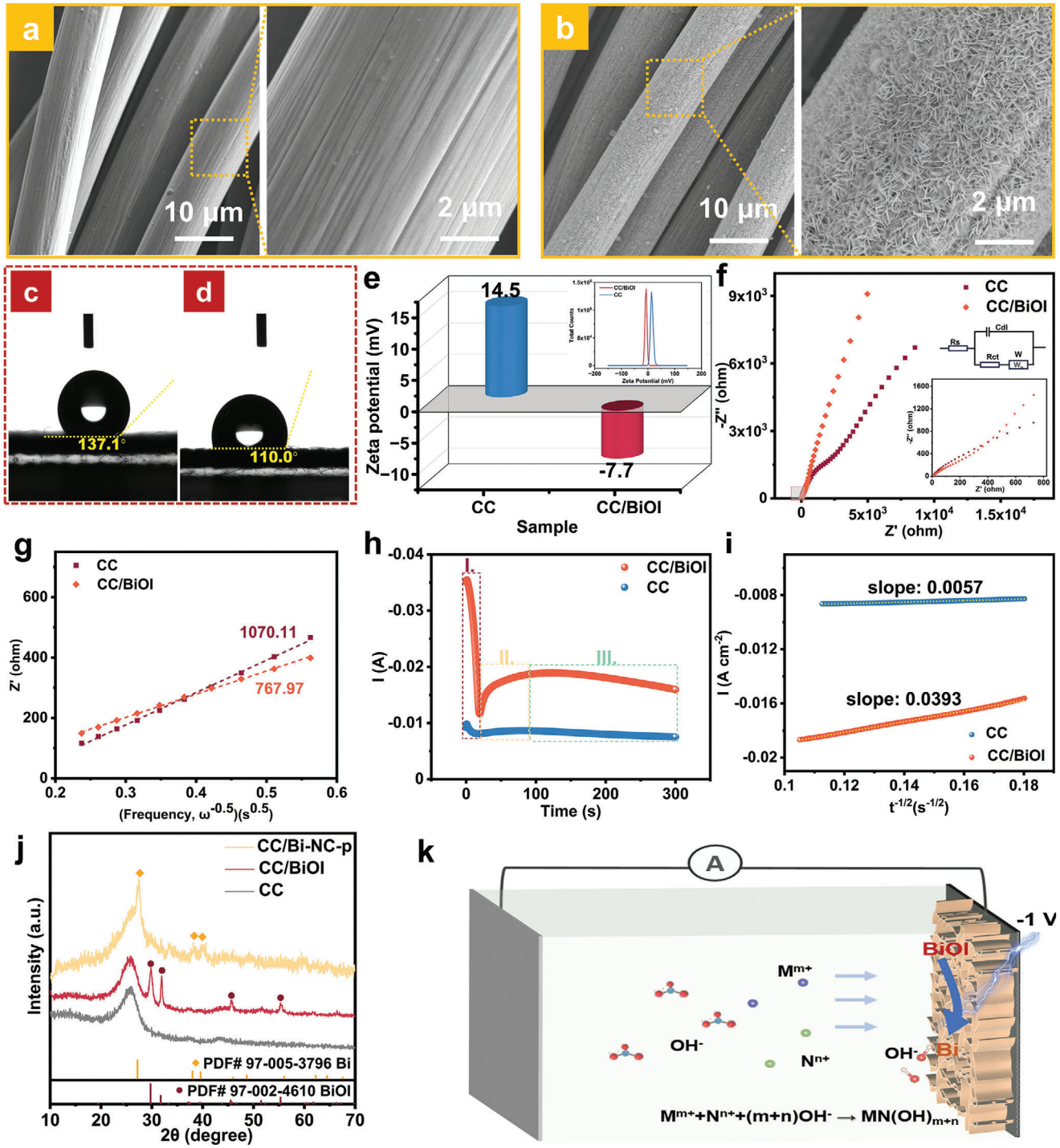

Figure 1. SEM images of a) bare CC and b) CC/BiOI. Contact angle images of c) CC and d) CC/BiOI. e) Zeta potentials of CC and CC/BiOI. f) Nyquist plots and g) the real part (Z′) versus the reciprocal of the square root of frequency ($\omega^{-0.5}$) in the intermediate frequency range. h) i–t curve and i) current density–$t^{-1/2}$ curve during electrodeposition of NC-p. j) XRD patterns of CC/BiOI before electrodeposition of NiCo hydroxide and NiCo hydroxide-precursor (CC/Bi-NC-p) after electrodeposition. k) Schematic illustration of electrodeposition of NiCo hydroxide.

slope of the Z' (real part of the complex impedance) and the $\omega^{-0.5}$ (angular frequency), and the results are presented in Figure 1g. The lower diffusion resistance of CC/BiOI than that of CC indicates rapid diffusion of metal cations. Therefore, BiOI NAs may provide more reaction sites for subsequent electrodeposition processes than the smoother bare CC fibers.

To clarify the differences between the electrodeposition processes of both samples, the current–time (i–t) curves of electrodeposition of NiCo hydroxide precursors as substrates were studied. Figure 1h exhibits that the chronoamperometry curves of both samples can be divided into three stages. In stage (I), the process of rapid double-layer charging increased the current speed, as well as the rapid current attenuation caused by the completion of double-layer charging. In this stage, nucleation of crystals did not occur on the electrode surface; however, it started in stage (II). During the growth of independent nucleating crystals or simultaneous generation of new nuclei, the growth of crystal nucleus led to the increase in the current on the electrode to reach a maximum value in stage (II). During stage (III), the electrodeposition current slowly declined as the planar infinite diffusion of the electrode surface gradually extended to the depth of the solution.[25] CC/BiOI displayed a significantly higher current response than CC, indicating better growth kinetics of NiCo-hydroxide materials on its surface.[26] According to the relationship between current density and time in the electrodeposition process (Equation (1),[27]) the diffusion coefficient (D) of the electrodeposited ions can be determined by the slope of the line obtained by plotting the current density versus $t^{-1/2}$ (Figure 1i).

$$I = \frac{nFD^{1/2}C_{ox}^{*}}{\pi^{1/2}t^{1/2}} \quad (1)$$

where I represents the current density (A cm^{-2}), n is the electron transfer number, F refers to the Faraday constant (96485 C mol^{-1}), C_{ox}^{*} is the bulk concentration of electrolyte (mol cm^{-3}), and t denotes deposition time (s). Table S2 (Supporting Information) presents that the diffusion coefficient of electroactive ions (Co^{2+}, Ni^{2+}) on CC/BiOI (5.791×10^{-18}) was significantly greater than that on CC (1.201×10^{-19}). This can explain the uniform distribution and higher mass loading of NiCo hydroxide electrodeposited on CC/BiOI.

X-ray diffraction (XRD) patterns before and after electrodeposition of NiCo hydroxide precursors are shown in Figure 1j. After the electrodeposition of nickel cobalt hydroxide, the characteristic peaks of BiOI (PDF# 97-002-4610) at 29.7, 31.7, 45.5, and 55.3° are no longer observed in the pattern of CC/Bi-NC-p. However, distinct peaks corresponding to (012), (104), and (110) crystallographic planes of Bi (PDF# 97-005-3796) appear at 27.2, 38.0, and 39.6° respectively. The pure NiCo hydroxide precursor was characterized by powder XRD (PXRD) and transmission electron microscopy (TEM)/high-resolution TEM (HRTEM) (Figure S3, Supporting Information), and the results show the presence of partial crystal structure and low crystal quality. Obviously, BiOI transformed into metallic Bi during electrodeposition due to the electrodeposition potential of NiCo hydroxide precursors being at −1 V, at which BiOI could be reduced to metallic Bi.[28] The conversion of BiOI to Bi can be described as follows: $BiOI + H_2O + 3e^- \rightarrow Bi + I^- + 2OH^-$. This enhanced the local OH^- ion concentration on the electrode surface, kinetically driving the deposition of metal hydroxide.[29] Schematic illustration presented in Figure 1k exhibits that transformation of BiOI into Bi favored the electrodeposition kinetics of NiCo-hydroxide precursors. Therefore, CC/BiOI promoted the electrodeposition of NiCo-hydroxide precursor to maintain higher mass loading and uniformity than CC. After the second electrodeposition, the hierarchical CC/Bi-NC-p electrodes and the morphology of the Bi-interlayer were clearly revealed by cross-section scanning electron microscopy (SEM) image and line/surface scan energy-dispersive spectroscopy (EDS) spectrum (Figure S4, Supporting Information).

2.2. Morphology and Structural Characterization

The influence of the Bi interlayer on the distribution of NCP in the outer layer was studied by SEM, and the results of CC/NCP (no Bi interlayer) and CC/Bi-NCP-2 (containing Bi interlayer) are shown in **Figure 2**a,b. The NCP of both samples consisted of many interwoven nanosheet arrays. However, the NCP layer of the sample without a Bi interlayer was discontinuous (Figure 2a), while the bare carbon CC was formed in many places. By contrast, the NCP layer of the CC/Bi-NCP-2 sample displayed dense distribution with good and continuous uniformity (Figure 2b), attributed to the initial role of BiOI NAs in facilitating the electrodeposition of NiCo hydroxide (precursor of NCP). The uneven distribution of the material on the substrate surface may cause the slow or even discontinuous migration of electrolyte ions to the electrode.[17] Therefore, the uniform and continuous distribution of NAs of CC/Bi-NCP-2 may ensure the smooth migration of ions. Moreover, the load mass of the active substance of CC/Bi-NCP-2 (3.5—5 mg) was much higher than that of CC/NCP (0.7–1.2 mg), conducive to achieve high area capacitance. Besides, the SEM images and EDS spectra of CC/Bi (Figures S5 and S6, Supporting Information) showed changes in Bi from NAs to particle arrays (PAs) after annealing treatment.

The multi-layered structure between the Bi interlayer and NCP outer layer of the CC/Bi-NCP sample was characterized by analyzing the cross-section SEM images of the electrodes (Figure S7, Supporting Information). Multilayered structures tended to form higher specific surface areas, as confirmed by nitrogen absorption and desorption tests (Figure S8, Supporting Information). The CC/Bi-NCP-2 multi-layer heterostructure possessed a larger specific surface area, abundant mesoporous structure, and larger total pore volume than CC/NCP, conducive to faster mass transfer during electrochemical reactions.

The elemental composition of CC/Bi-NCP-2 was evaluated by detaching the deposited film from CC fibers by ultrasonic treatment, followed by characterization through scanning transmission electron microscopy (STEM, Figure 2c) and EDS (Figure 2d). The formed nanosheets consisted of many fine particles (STEM image in Figure 2c). Moreover, the elemental mapping revealed the upper left region with a prominently higher concentration of Bi element, indicating the formation of a heterostructural interface between Bi and NCP within this area. The EDS analysis results shown in Figure 2d confirm the presence of Bi, Co, Ni, and P elements in CC/Bi-NCP-2 samples. Both EDS and inductively coupled plasma (ICP) spectrometry showed a Co:Ni ratio close to

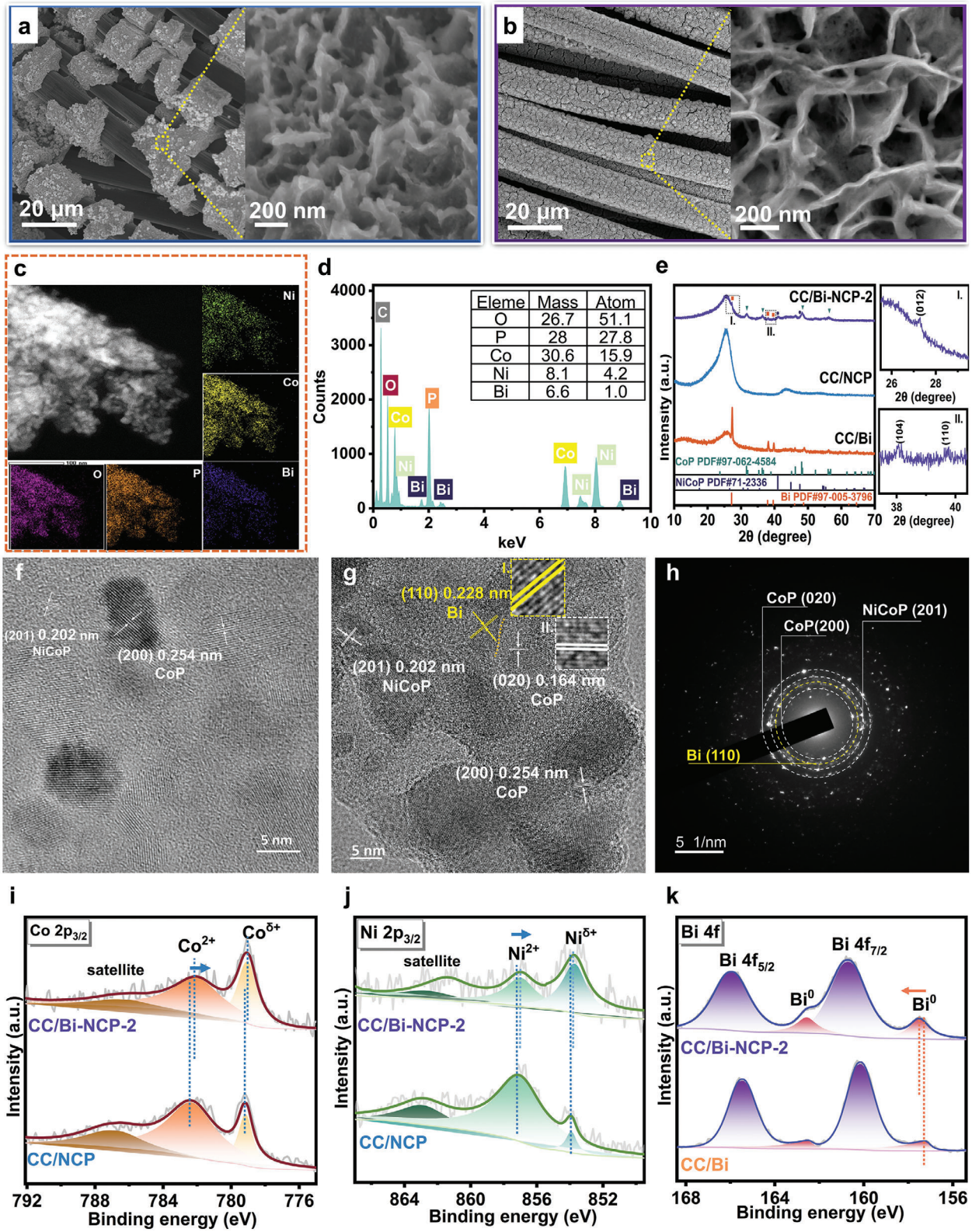

Figure 2. SEM images of a) CC/NCP and b) CC/Bi-NCP-2. c) STEM image with the corresponding mapping elements and d) EDS of CC/Bi-NCP-2. e) XRD patterns of CC/Bi-NCP-2 and contrast samples. HRTEM images of f) CC/NCP and g) CC/Bi-NCP-2. h) SAED pattern of CC/Bi-NCP-2. High-resolution XPS spectra of i) Co $2p_{3/2}$, as well as j) Ni $2p_{3/2}$ of CC/Bi-NCP-2 and CC/NCP. k) High-resolution XPS spectra of Bi 4f of CC/Bi-NCP-2 and CC/Bi.

3:1 (Table S3, Supporting Information), indicating a significant amount of cobalt phosphide alongside NCP with higher content.

The XRD patterns of CC/Bi-NCP-2, CC/NCP, and CC/Bi are shown in Figure 2e. The peaks located at 27.16°, 37.99°, and 39.58° for the CC/Bi sample corresponded to (012), (104), and (110) faces of the hexagonal Bi (PDF#97-005-3796). The low mass loading and crystallinity of NCP in CC/NCP samples resulted in no obvious diffraction peaks. By comparison, the peaks near 40.99° and 47.58° in the CC/Bi-NCP-2 sample were assigned to the (111) and (210) faces of hexagonal NiCoP (PDF#97-071-2336). The peaks near 31.60°, 36.67°, 48.38°, and 56.03° can be attributed to (011), (102), (202), and (020) faces of the orthogonal CoP (PDF#97-062-4584). The weak and broad diffraction peaks of CoP and NCP in CC/Bi-NCP-2 samples indicate poor crystallization characteristics, which may be related to the temperature and time of the phosphating process. The local magnification I and II of the XRD pattern of CC/Bi-NCP-2 reveal the presence of Bi (102), (104), and (110) faces. The peak intensity was low due to the modest Bi inside the sample.

The presence of heterostructures of CC/NCP and CC/Bi-NCP was further demonstrated by HRTEM analysis. Figure 2f exhibits the presence of NiCoP (201) and CoP (200) planes for CC/NCP samples, indicating the presence of both CoP and NCP phases in NCP sample. Previous studies pointed out the co-existence of NCP and CoP in NCP sample obtained from phosphating the hydroxide precursor,[30] conducive to enhanced electrochemical properties. For instance, Hu et al. examined the interaction between CoP and NCP by generating a built-in electric field that accelerated electron mobility and improved multiple properties.[31] Notably, the synergies of NCP and CoP have been discussed in previous study, thus, they were not considered herein. The HRTEM image of the CC/ Bi-NCP sample in Figure 2g exhibits the presence of (201) plane of NiCoP, (200) and (020) planes of CoP, and the heterointerface of CoP (020) and Bi(110) planes all locally enlarged in regions I and II. The selected-area electron diffraction (SAED) pattern of the CC/Bi-NCP sample (Figure 2h) and TEM image of the selected area (Figure S9, Supporting Information) illustrate polycrystalline characteristics, indicating the presence of NCP, CoP, and Bi phases. The Raman spectra shown in Figure S10 (Supporting Information) also exhibit the presence of Bi metal in CC/Bi-NCP-2, consistent with the XRD and HRTEM results.

The changes in chemical valence and electronic state caused by the formation of heterostructure were explored by X-ray photoelectron spectroscopy (XPS). The full scan spectra of CC/Bi, CC/NCP, and CC/ Bi-NCP-2 (Figure S11, Supporting Information) exhibit the presence of Co, Ni, P, O, C, and Bi elements in CC/Bi-NCP-2 samples. Figure 2i shows the presence of a total of three Co $2p_{3/2}$ peaks at 779.2, 782.4, and 781.1 eV for CC/NCP, attributed to $Co^{\delta+}$ from CO−P, Co^{2+} from Co−PO_X, and satellite peak,[30a] respectively. Moreover, the Co $2p_{3/2}$ energy level in CC/Bi-NCP-2 underwent a negative shift. Similarly, the high-resolution Ni $2p_{3/2}$ XPS spectra presented in Figure 2j show three peaks belonging to Ni–P, Ni–PO_X, and satellite peaks,[5] respectively. Further, CC-Bi-NCP-2 peaks underwent a negative shift relative to CC/NCP. The position of the P2p peak corresponding to the CC/Bi-NCP-2 sample also shifted to negative values when compared to the CC/NCP sample (Figure S10, Supporting Information). In the Bi 4f XPS spectra of CC/Bi (Figure 2k), the two low-intensity peaks at 162.5 and 157.3 eV could be assigned to the Bi−Bi bond, while the other two high-intensity peaks at 165.5 and 160.2 eV were linked to the Bi−O bond.[21] Compared to the CC/NCP sample, the position of the peak corresponding to the Bi−Bi bond of the CC/Bi-NCP-2 sample was slightly positive. In general, the binding energies of Ni, Co, and P elements in CC/ BI-NCP-2 were lower than those of CC/NCP, while the Bi element exhibited higher binding energy than CC/Bi, indicating electron redistribution between Bi and NCP.

2.3. Electrochemical Performance of Electrodes

To demonstrate the influence of Bi interlayer on the electrochemical energy storage of NCP, the electrochemical properties of CC/Bi-NCP-x (x = 1, 2, and 3), CC/NCP, and CC/Bi were evaluated in a three-electrode cell containing 6 M KOH electrolyte. **Figure 3a** illustrates that the cyclic voltammetry (CV) curves of both CC/NCP and CC/Bi-NCP-x (x = 1, 2, and 3) electrodes depict a clear pair of redox peaks, which can be attributed to Ni^{2+}/Ni^{3+} and $Co^{2+}/Co^{3+}/Co^{4+}$ Faraday reactions.[5] The possible reaction mechanism of electrodes can be expressed as follows:[32]

$$Ni^{\delta+} + 2OH^- \rightarrow Ni(OH)_2 + (2-\delta)\,e^- \quad (2)$$

$$Ni(OH)_2 + OH^- \leftrightarrow NiOOH + H_2O + e^- \quad (3)$$

$$Co^{\delta+} + 2OH^- \rightarrow Co(OH)_2 + (2-\delta)\,e^- \quad (4)$$

$$Co(OH)_2 + OH^- \leftrightarrow CoOOH + H_2O + e^- \quad (5)$$

$$CoOOH + OH^- \leftrightarrow CoO_2 + H_2O + e^- \quad (6)$$

Consistent with previous findings, the NiCo phosphide ($Ni^{\delta+}/Co^{\delta+}$) undergoes oxidation to form the corresponding hydroxide, followed by subsequent conversions between the hydroxide and hydroxy oxide species.[32] The characterization results of the sample after cycles (Figures S17 and S18, Supporting Information) also correspond to this. Comparative analysis indicates that the CC/Bi electrodes also showed rectangle-like curve within the same potential window, indicating no Faraday reactions of Bi in this potential interval, since Bi typically reacted in a negative potential interval under alkaline conditions.[21] The CC/Bi-NCP-2 electrode exhibited higher redox peaks and larger CV curve areas, suggesting stronger energy storage capacity than CC/Bi-NCP-1, CC/Bi-NCP-3, CC/NCP, and CC/Bi. This also shows that too little Bi in the heterostructure of Bi and NCP did not have any influence, while excessive Bi negatively impacted the overall performance of the electrode due to its low capacitance. Figure 3b demonstrates that both CC/NCP and CC/Bi-NCP-x (x = 1, 2, and 3) exhibited nonlinear galvanostatic charge/discharge (GCD) curves, while CC/Bi-NCP-2 illustrated the longest discharge time, corroborating the CV electrochemical measurements. The comparative analysis of specific capacitances of CC/NCP and CC/Bi-NCP-x (x = 1, 2, and 3) at different current densities is presented in Figure 3c. The CC/Bi-NCP-2 sample displayed significantly superior capacitance in a wide range of current densities, reaching 1200 F g^{-1} at 1 A g^{-1}. The rate capability of CC/Bi-NCP-2 was also

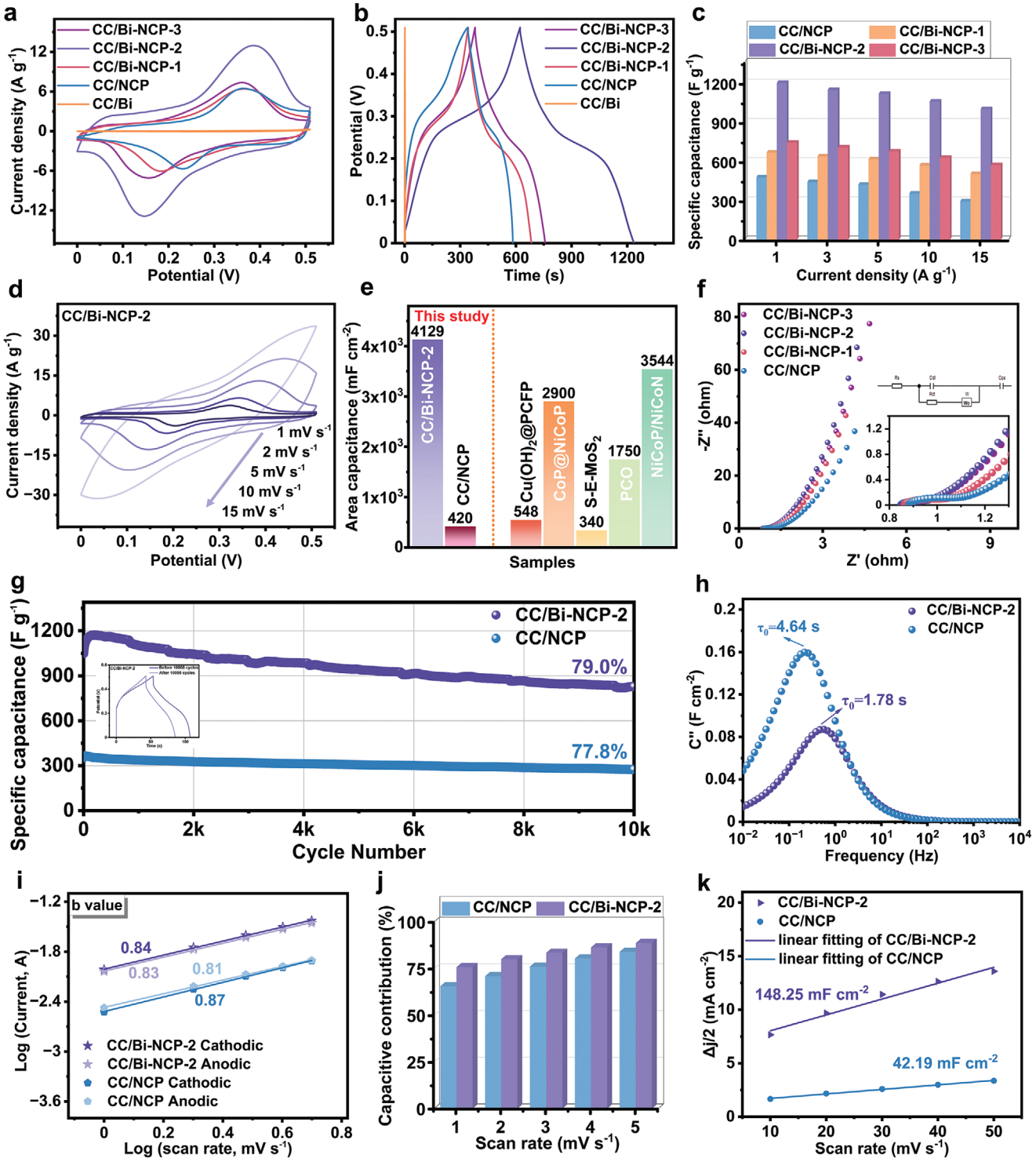

Figure 3. Comparison of a) CV curves, b) GCD profiles, and c) specific capacitances at different current densities of CC/Bi-NCP-x (x = 1, 2, and 3), CC/NCP and CC/Bi. d) CV curves at different scan rates of CC/Bi-NCP-2 sample. e) Area capacitance of CC/Bi-NCP-2 and other electrodes. f) EIS Nyquist plots of several samples. g) Cyclic stability for 10 000 cycles at 10 A g^{-1} (Inset: GCD profiles of CC/Bi-NCP-2 for the first and last cycles). h) Frequency responses of C″ of CC/NCP and CC/Bi-NCP- 2,. i) Calculation of power law exponents, and j) Capacitance contribution ratio histograms of CC/NCP and CC/Bi-NCP-2. k) C_{dl} values of CC/NCP and CC/Bi-NCP-2.

excellently maintained at 1000 F g^{-1} at 15 A g^{-1}. The GCD profiles of CC/Bi-NCP-2 under different current densities are presented in Figure S13 (Supporting Information). Obviously, the approximately symmetrical charge-discharge curve showed CC/Bi-NCP-2 possessing excellent Coulomb efficiency and reversible redox capacitance. As displayed in Figure 3d, the CV curves of CC/Bi-NCP-2 electrodes at different sweep speeds showed increased peak currents of the cathodic and anodic process as a function of scan rate. Additionally, the position of the peaks slightly shifted due to polarization at larger sweep speeds. Notably, Bi interlayer promoted the uniform and continuous deposition of NCP; therefore, CC/Bi-NCP-2 displayed higher active material load with an area-specific capacitance up to 4129 mF cm^{-2} at 1 mA cm^{-2}, a value significantly higher than that of CC/NCP (Figure 3e; Figure S14, Supporting Information). Moreover, the area–specific capacitance of the CC/Bi-NCP-2 electrode was superior to those of some reported TMPs/ transition metal sulfides (TMSs) electrode materials.[31,33]

The charge transfer and diffusion behaviors of different electrodes were further studied by EIS. The inset in Figure 3f shows the corresponding equiv. circuit diagram and local amplification of the high-frequency region. The specific values of the series resistance (Rs), charge transfer resistance (Rct), and Warburg impedance (Rw) of CC/Bi-NCP-x (x = 1, 2, and 3) and CC/NCP are listed in Table S4 (Supporting Information). All the CC/Bi-NCP-x (x = 1, 2, and 3) samples showed Rs values lower than that of CC/NCP, indicating a smaller intrinsic resistance of the electrode after the introduction of Bi. The significantly reduced Rct value of CC/Bi-NCP-2 (0.079 Ω) when compared to CC/NCP (0.374 Ω) indicated enhanced charge transfer ability. Moreover, CC/Bi-NCP-2 electrode displayed the lowest Rw and diffusion resistance σ (Figure S15, Supporting Information) compared to CC/NCP, CC/Bi-NCP-1, and CC/Bi-NCP-3, inferring the lowest ion diffusion resistance and faster ion diffusion of CC/Bi-NCP-2. In cyclic stability tests at 10 A g^{-1} (Figure 3g), CC/Bi-NCP-2 displayed lasting stability with a 79.0% retention rate after 10 000 cycles, a value slightly better than that of CC/NCP (77.8% retention rate after 10 000 cycles). Besides, the cyclic process did not cause more instability due to the introduction of Bi. The SEM image of CC/Bi-NCP-2 after 10 000 charge–discharge cycles is shown in Figure S16 (Supporting Information). After the cyclic test, the morphology was still maintained without collapsing. The structure and chemical state of the CC/Bi-NCP-2 electrode after the cycle stability test were analyzed by XRD, Raman spectroscopy, HRTEM, and XPS (Figures S17 and S18, Supporting Information). After the long-term electrochemical test, the NCP underwent oxidation and transformed into the corresponding hydroxide/hydroxyl oxide species, which is consistent with previous results[31,34] and this is also the reason for the deterioration of electrode stability.

The evolution of C´´as a function of frequency is illustrated in Figure 3h. Noteworthy, the operating frequency f_0 is related to the relaxation time constant τ_0 ($\tau_0 = 1/f_0$), where τ_0 represents the release of energy greater than 50% efficiency.[35] The τ_0 of CC/Bi-NCP (1.78 s) was lower than that of CC/NCP (4.64 s), indicating a faster response time, consistent with its efficient ion diffusion and high-rate capability. The charge storage mechanism of the CC/Bi-NCP-2 electrode was studied by CV testing at scanning rates of 1–5 mV s^{-1} (Figure S19, Supporting Information), with the b value calculated by using Equation (7) as follows:

$$i = av^b \tag{7}$$

where i represents the peak current, v is the scan rate, and a and b are constants.[8a]

For b ≤ 0.5, the mechanism is controlled by diffusion, while b = 1 indicates a capacitance-controlled energy storage mechanism. The anode/cathode processes of CC/Bi-NCP-2 and CC/NCP both showed b values of 0.83 and 0.84 (Figure 3i). Its b value was observed to be between 0.5 and 1 (greater than 0.8), which indicates that the electrode shows both diffusion and capacitance-controlled behavior and that the surface redox reaction is dominant.[1,36]

The contribution rates of both behaviors were calculated by using Equation (8), as follows:

$$i = k_1 v + k_2 v^{1/2} \tag{8}$$

where $k_1 v$ and $k_2 v^{1/2}$ represent capacitance and diffusion contributions, respectively.[33a]

Figure 3j illustrates that the capacitance effects of both CC/Bi-NCP and CC/NCP electrodes increased as a function of the scan rate, due to the limited reaction time of electrons with the active material. This, in turn, enhanced the surface-confined capacitance. However, even at a lower sweep speed of 1 mV s^{-1}, the capacitance contribution of the CC/Bi-NCP-2 electrode was still close to 75%, indicating a capacitance contribution brought by its unique structure that enhanced the reaction kinetics, resulting in remarkable electrochemical performance.

The electrochemical active surface area (ECSA) of the electrode material was determined by calculating the double-layer capacitance (C_{dl}). Figure 3k shows that CC/Bi-NCP-2 exhibited a larger C_{dl} of 148.25 mF cm^{-2} (Figure S20, Supporting Information). The ECSA of the electrode was calculated by using Equation (9),[37] as follows:

$$ECSA = \left(\frac{C_{dl}}{C_s}\right) A_{geo} \tag{9}$$

where Cs is constant of 0.04 mF cm^{-2} in an alkaline electrolyte,[38] and A_{geo} is the geometric area of the electrode (1 cm^2). According to the calculation, the ECSA value of CC/Bi-NCP-2 is 3706.2 cm^2, which is larger than that of CC/NCP (1054.8 cm^2), proving the introduction of additional electrochemically active sites introduced by the constructed Bi-NCP hierarchical heterostructure, resulting in significantly enhanced energy storage performance.

2.4. Effects of Heterostructure

The influences of Bi on the structures and electrochemical properties of CC/Bi-NCP-2 were studied by density functional theory (DFT) calculations combined with experimental results. According to theoretical calculations, the work functions of Bi, CoP, and NiCoP were determined as 4.249, 4.438, and 4.672 eV, respectively (Figure S21, Supporting Information). The corresponding values of Fermi energy (E_f) were estimated to be −4.249, −4.438,

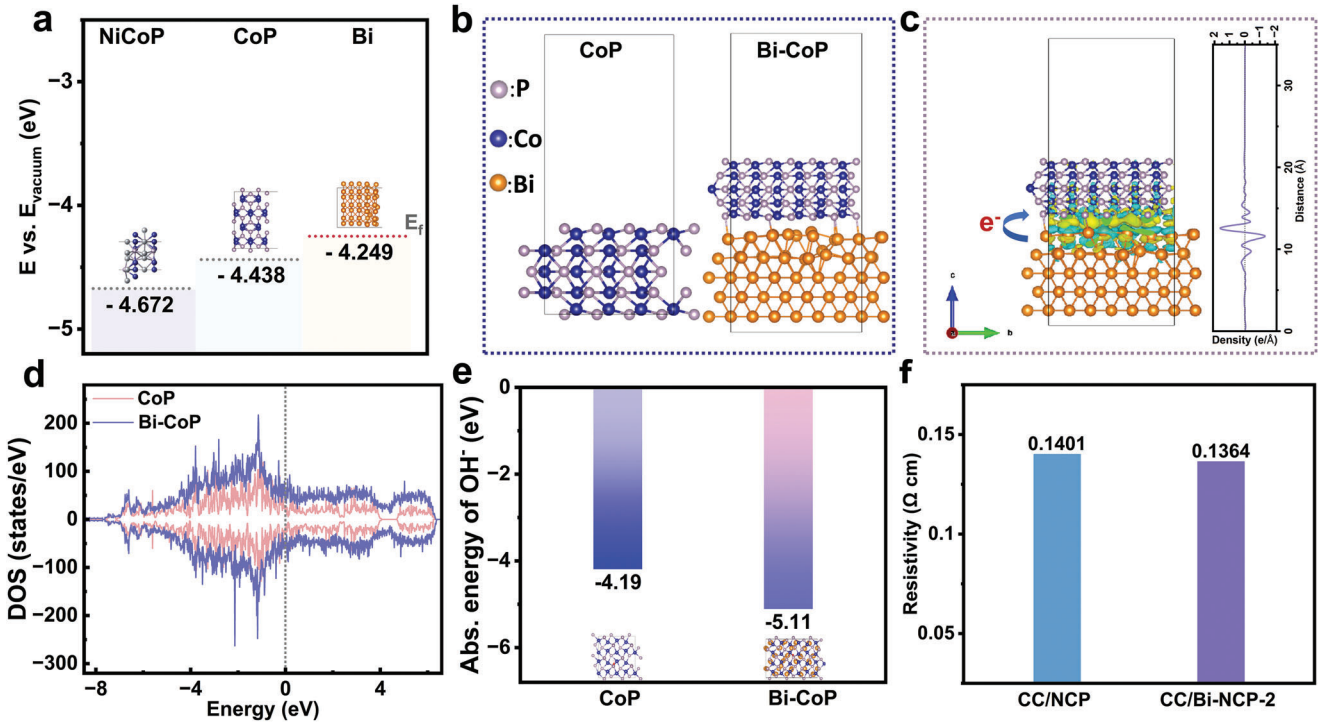

Figure 4. a) Fermi-level illustrations of NiCoP, CoP, and Bi. b) Atomic structure models of CoP and Bi-CoP heterostructures. c) Charge density difference at Bi-CoP heterostructure interface (yellow areas represent charge accumulation and green areas represent charge depletion). d) The TDOS of CoP and Bi-CoP. e) The adsorption energies of OH^- in CoP and Bi-CoP. f) Resistivity features of CC/NCP and CC/Bi-NCP-2.

and −4.672 eV (vs vacuum), respectively (**Figure** 4a). Notably, electrons migrated from materials with high E_f to materials with low E_f when different phases were in contact;[39] therefore, electrons in the Bi interlayer of CC/Bi-NCP electrodes would theoretically migrate to the outer layer of CoP and NiCoP. A heterostructure model of Bi-CoP was constructed by considering the following conditions. i) The content of CoP components in CC/Bi-NCP-2 was significantly higher than NiCoP (EDS results in Figure 2). ii) Complex construction and calculation of a model containing three phases of Bi, CoP, and NiCoP. iii) Interaction between CoP and NiCoP was not the main research direction of this study. CoP was then used as a model for comparative analysis (Figure 4b). Based on HRTEM analyses (Figure 2), the exposed facets of CoP and Bi were selected as (200) and (110), respectively. Charge density difference simulations were then implemented to further comprehend the effect of the built-in electric field on charge transfer within the heterostructure of Bi-CoP (Figure 4c). Noteworthy, the difference in charge density reflected the unbalanced charge distribution at the interface of Bi-CoP heterostructure and significant charge transfer from Bi to CoP. In other words, the yellow areas in Figure 4c represent gained electrons while lake blue areas represent lost electrons.

The values of the total density of states (TDOS) of CoP and Bi-CoP are shown in Figure 4d, and those of the projected density of states (PDOS) are illustrated in Figure S22 (Supporting Information). Compared to CoP, the increase in state density near the Fermi level (the Fermi energy was shifted to 0 eV) of Bi-CoP indicated a change in electronic structure conducive to rapid charge transport, implying stronger conductivity for good rate capability of the electrode. Moreover, the heterogeneous interface effect revealed narrowed d-band center values from CoP (−1.365 eV) to Bi-CoP (−12.044 eV), providing a lower electron/ion transfer barrier and easier electron excitation.[40] Furthermore, the adsorption energy of the electrode material toward OH^- ions would also be an important indicator of the redox reaction barrier. The reason for this had to do with the charging of the electrode, which would capture OH^- ions in the electrolyte and convert them into the final high-priced product and H_2O after the completion of the redox reaction. The model diagrams of Bi-CoP and CoP after the adsorption of OH^- ions are provided in Figure S23 (Supporting Information). Figure 4e exhibits that the adsorption energy of Bi-CoP was lower than that of CoP, indicating a more helpful heterogeneous interface for the adsorption of OH^- ions. Moreover, the heterogeneous interface was more conducive to the diffusion of electrolyte ions, promoting the redox reaction corresponding to the stronger charge storage capacity of CC/Bi-NCP-2. The resistivity test results of the two materials shown in Figure 4f confirm the lower resistivity of CC/Bi-NCP-2 than that of CC/NCP. In other words, the electronic conductance of CC/Bi-NCP enhanced, corroborating DOS calculations.

Overall, the combination of theoretical calculations and experimental results proves that the construction of reasonable heterostructure (CC/Bi-NCP-2) through Bi interlayer can effectively enhance the charge transfer at the interface and improve the electron conductance, which is conducive to the occurrence of improved electrochemical reactions at the electrodes. The significantly enhanced electrochemical energy storage capacity of CC/Bi-NCP-2 electrodes can be attributed to the constructed

hierarchical heterogeneous structures through the "Bi-interlayer" strategy, leading to several advantages. i) The electrodeposition kinetics of NC-p (NiCo hydroxide) through the constructed Bi-interlayer formed uniform and continuous nanoarray active material on the CC fiber, promoting the mass loading of the active material per unit area for achieving high area specific capacitance and ensuring unobstructed ion transport of the electrolyte. ii) The multi-layered Bi-NCP heterostructure increased the specific surface area and formed a more abundant pore structure with active sites, providing a larger reaction area for electrolyte ions for rapid redox reaction kinetics. iii) A strong interface effect was achieved between the "Bi-interlayer" and "NCP outer layer", generating an internal electric field for accelerated electron transport and promoting the adsorption of OH^- ions. These features reduced the resistance of electron conduction and ion diffusion, resulting in excellent supercapacitor performance.

2.5. Electrochemical Performance of Assembled Supercapacitors/Alkaline Zn Battery Devices

The CC/Bi-NCP-2 was used as positive electrode due to its excellent electrochemical performance, and it was assembled with two negative electrodes of sucrose-derived carbon (SDC) and Bi_2O_3 to form an HSC and supercapattery. The SDC obtained by the rapid redox reaction of concentrated sulfuric acid and sucrose formed defects in the carbon material with a large number of inserted heteroatoms, leading to remarkable electrochemical properties when compared to the commercially available activated carbon (Figure S24, Supporting Information). The CV curves of positive (CC/Bi-NCP-2) and negative (SDC) electrodes under 5 mV s^{-1} are provided in **Figure 5a**. SDC showed a quasi-rectangular CV curve with a working potential of −1 to 0 V, while CC/Bi-NCP-2 displayed a Faraday-type CV curve with a working potential of 0–0.51 V. The CV curves of CC/Bi-NCP-2||SDC HSC under different potential windows are displayed in Figure S25 (Supporting Information). The results indicate that its stable operating potential window could be set to 1.6 V. Figure 5b exhibits that the CV curves of the designed HSC device maintained a stable shape as a function of scan rate, showing good Coulombic efficiency and excellent reversibility. The GCD profiles and calculated specific capacitances of CC/Bi-NCP-2||SDC HSC device at current densities from 1 to 20 A g^{-1} are exhibited in Figure S26 (Supporting Information) and Figure 5c, respectively. CC/Bi-NCP-2||SDC HSC device achieved a specific capacitance of 181.06 F g^{-1} at 1 A g^{-1}, with 42.1% maintained capacity even at a super high current density of 20 A g^{-1}. Figure 5d shows the Ragone diagram, which exhibits that the assembled HSC device achieved an energy density of 64.4 Wh kg^{-1} at a power density of 1600 W kg^{-1}, better than that for reported supercapacitor devices assembled with NiCo-based positive and carbon material negative electrodes (Table S5, Supporting Information).[5,30c,35,41] After 10 000 charge and discharge cycles (Figure 5e), CC/Bi-NCP-2||SDC HSC showed a capacitance retention rate of 78.68% with excellent Coulombic efficiency close to 100%, showing durable electrochemical stability and good reversibility.

Bi_2O_3 material was used as a negative electrode, which could further improve the energy density of the device by relying on its suitable potential window and significantly better capacity than carbon materials. The electrochemical properties of the as-prepared Bi_2O_3 negative electrode are presented Figure S27 (Supporting Information). Figure 5f shows that Bi_2O_3 presents a Faraday-type CV curve with a working potential of −1 to 0 V, while CC/Bi-NCP-2 displays the same CV curve as shown in Figure 5a. The CV tests performed on devices with different potential windows revealed a stable operating potential window of 0–1.6 V (Figure S28, Supporting Information). The CV curves of the CC/Bi-NCP-2||Bi_2O_3 device at different scan rates possessed prominent redox peaks (Figure 5g), corresponding to obvious discharge plateaus in GCD profiles (Figure S29, Supporting Information), implying battery-like characteristics due to the Faraday reactions of metal species. Figure 5h illustrates that the specific capacitances of CC/Bi-NCP-2||Bi_2O_3 device were determined to be 230.3 F g^{-1} at 1 A g^{-1} and 51.3 F g^{-1} at 20 A g^{-1}. As indicated by Ragone plots shown in Figure 5i, the assembled CC/Bi-NCP-2||Bi_2O_3 device delivered an energy density of 81.8 Wh kg^{-1} at a power density of 1600 W kg^{-1}. This can be seen as an advanced level of the same type of devices, such as combinations of NiCo-based materials for the positive electrode and metal oxides for the negative electrode. The detailed data are listed in Table S6 (Supporting Information).[8b,42] After 5 000 charge and discharge cycles at the current density of 10 A g^{-1} (Figure 5j), the capacitance retention rate of the CC/Bi-NCP-2||Bi_2O_3 device reached 67.5% and the corresponding Coulombic efficiency was close to 92%. The photographs of the CC/Bi-NCP-2||SDC and CC/Bi-NCP-2||Bi_2O_3 devices are provided in Figure S30 (Supporting Information).

To further increase the energy density, AZB devices (CC/Bi-NCP-2||Zn pouch cell) composed of 3 M KOH and 0.1 M $Zn(CH_3COO)_2$ electrolyte, Zn anode, and CC/Bi-NCP-2 cathode were assembled (inset of **Figure 6a**; Figure S31a, Supporting Information). Since the potential of the Zn metal electrode was more negative than that of carbon materials and Bi oxide (Figure S31b, Supporting Information), the voltage of CC/Bi-NCP-2-based AZB was 1.95 V (Figure 6a,b), a value higher than that of HSC. Moreover, the higher output voltage would be more practical for application. Figure 6a shows the CV curves of the assembled AZB in the potential window between 1 and 1.95 V. Clear redox peaks were observed originating from the interaction of the Faraday reactions (cathode: $Ni^{2+} + Co^{2+} \leftrightarrow Ni^{3+} + Co^{4+}$, anode: $Zn(OH)_4^{2-} \leftrightarrow Zn$). Additionally, no significant shape distortion was noticed with the increase in scan rate.

The charge and discharge curves of CC/Bi-NCP-2||Zn cells at different current densities are provided in Figure 6b. All curves exhibited a distinct 1.6–1.75 V discharge platform with negligible voltage hysteresis. Figure 6c presents that the rate profile of CC/Bi-NCP-2||Zn cell showed specific capacities ranging from 191.1 mAh g^{-1} at 1 A g^{-1} to 124.4 mA h g^{-1} at 20 A $^{-1}$, indicating excellent rate capability. The study of electrochemical reaction kinetics (Figure S31c–S31f, Supporting Information) revealed favorable electrode kinetics of CC/Bi-NCP-2||Zn battery.

The energy density and power density were calculated according to the discharge curves, and the results are shown in Figure 6d. Obviously, the CC/Bi-NCP-2||Zn battery provided a maximum energy density of 319.12 Wh kg^{-1} at a power density of 1.65 kW kg^{-1}. At power density reaching 33.01 kW kg^{-1}, the energy density was still maintained at 207.79 Wh kg^{-1}.

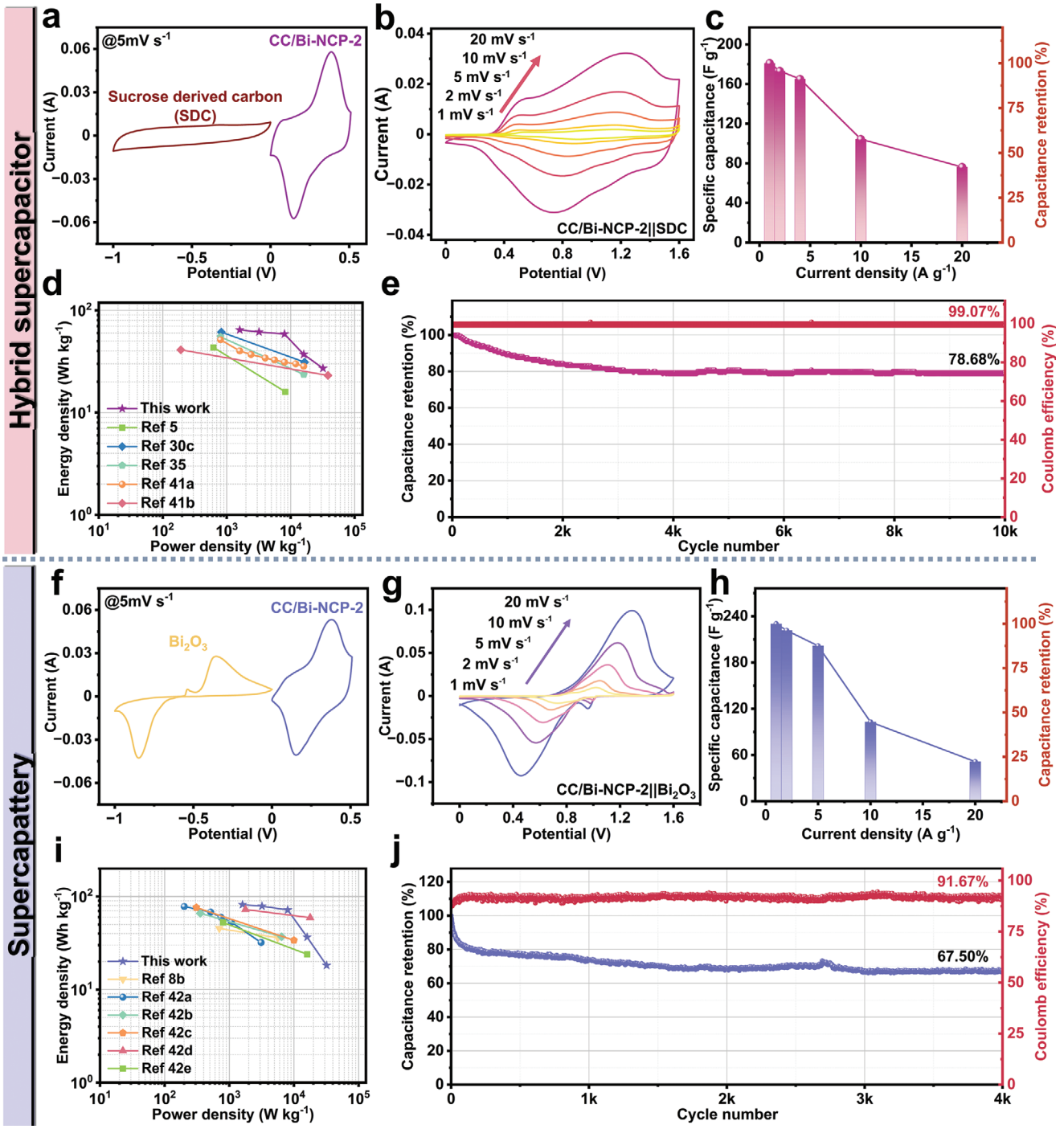

Figure 5. Electrochemical performance of CC/Bi-NiCP-2-based HSC devices: a) CV curves of positive electrode (CC/Bi-NCP-2) and negative electrode (SDC), b) CV curves of device at different scan rates, c) rate capability, d) Ragone plots, and e) cycle stability and coulombic efficiency of CC/Bi-NCP-2||SDC. f) CV curves of positive electrode (CC/Bi-NCP-2) and negative electrode (Bi_2O_3), g) CV curves of device at different scan rates, h) rate capability, i) Ragone plots, and j) cycle stability and coulombic efficiency of CC/Bi-NCP-2||Bi_2O_3.

Moreover, the overall performance of the AZB exceeded those of some previously reported Ni/Co-based AZBs (Figure 6d; Table S7, Supporting Information).[7,43] Further, the durability of CC/Bi-NiCoP//Zn batteries checked by GCD testing for 5 000 cycles at 10 A g^{-1} (Figure 6e) suggested capacity retention of AZB battery of 80.56%, showing good durability as a rechargeable battery. Attributed to the high operating voltage of AZB, a CC/Bi-NiCoP//Zn pouch cell was also able to light a red LED bulb for more than 20 min (Figure 6f), demonstrating a certain practicality.

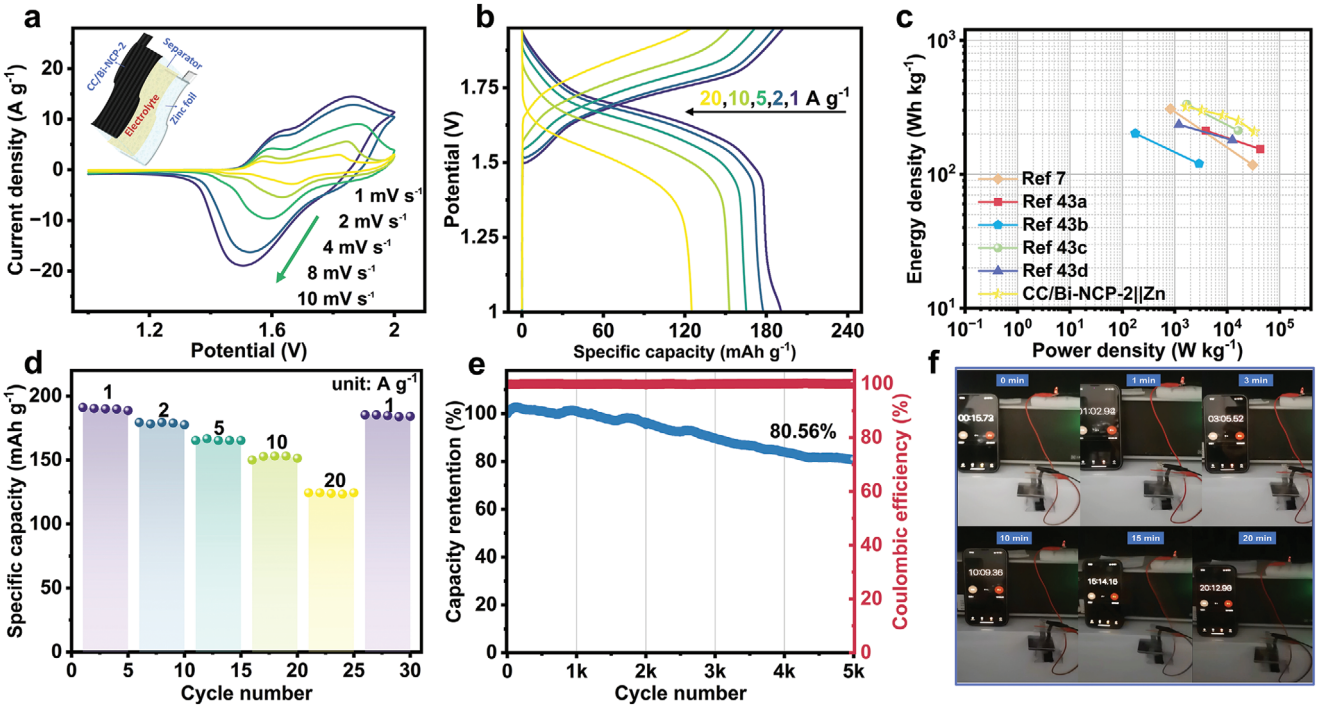

Figure 6. Electrochemical performance of the as-prepared CC/Bi-NCP-2||Zn AZB device: a) CV curves at various scan rates (inset shows a schematic illustration of AZB device), b) GCD curves at different current densities, c) rate capability, d) Ragone plots of CC/Bi-NCP-2 compared with those of some previously reported AZB devices, and e) cycle stability at 10 A g^{-1}. f) Device with continuous supply of power to LED bulb for 20 min.

The universality of the Bi-interlayer strategy was confirmed by preparing CC/Bi-nickel cobalt oxide (CC/Bi-NCO) for comparison with the CC/NCO sample (Figure S32, Supporting Information). Similar to CC/Bi-NCP, the sample CC/Bi-NCO showed significantly higher specific capacitance than CC/NCO and maintained durable cycle stability. Therefore, the Bi interlayer strategy not only affected NCP, but also positively influenced the electrochemical properties of NiCo oxides. Therefore, the proposed strategy possesses a certain universality, promising for future research and development.

3. Conclusions

A novel heterostructured CC/Bi-NCP electrode with outstanding electrochemical performance was successfully prepared by implementing a facile interlayer approach. By modifying the surface state of the substrate and enhancing electrodeposition kinetics, the Bi-interlayer increased the number of active sites for nucleation and growth of subsequent NiCo-hydroxide precursor. This ensured the formation of a continuous, uniform, and high-mass loading electrode with enhanced area capacitance. Experimental results and DFT calculations demonstrated that the formation of heterostructure engineering between Bi and NCP effectively enhanced the capacitance and rate performance by inducing an internal electric field to modulate charge distribution, facilitate electron migration, and promote OH^- adsorption and diffusion. HSC and supercapattery devices were then assembled using CC/Bi-NCP-2 as the positive electrode, and SDC and Bi_2O_3 as negative electrodes, respectively. The devices showed impressive energy densities of 64.4 and 81.8 Wh kg^{-1} combined with a remarkable power density of 32000 W kg^{-1}, respectively. Furthermore, the incorporation of Zn foil resulted in a pouch AZB with a significant energy density of 319.1 Wh kg^{-1}, demonstrating feasible practicality. Overall, the proposed interlayer strategy shows potential prospects for the future construction of multi-layer composites for heterostructured electrodes with high electrochemical performance.

4. Experimental Section

Chemicals: Bismuth nitrate pentahydrate ($Bi(NO_3)_3{\cdot}5H_2O$), ethanol (CH_3CH_2OH), acetone (CH_3COCH_3), p-benzoquinone ($C_6H_4O_2$), nitric acid (HNO_3), ammonium iodide (NH_4I), cobalt nitrate hexahydrate ($Co(NO_3)_2{\cdot}6H_2O$), nickel nitrate hexahydrate ($Ni(NO_3)_2{\cdot}6H_2O$), sodium hypophosphite monohydrate ($NaH_2PO_2{\cdot}H_2O$), potassium hydroxide (KOH), and Zn acetate dihydrate ($C_4H_6O_4Zn{\cdot}2H_2O$) were all purchased from Sinopharm Chemical Regent Co., Ltd. All the chemicals used were of AR grade and used as received without any further purification. The carbon cloth (CC, W0S1011) used was produced by CeTech Co., Ltd. High purity Zn foil was provided by Chengshuo Metal Materials Co., Ltd. The water used in the experiment was deionized water, which was obtained in the laboratory using a water purification system.

Preparation of CC/Bi-NCP and CC/NCP: The preparation process of CC/Bi-NCP consisted of two-step electrodeposition and phosphating annealing. First, CC/bismuth oxyiodide (BiOI) was prepared by electrodeposition on CC according to previously reported methods.[44] To study the effects of different Bi contents, the deposition time of BiOI was set to 100, 200, and 300 s, respectively. Next, CC/Bi-NiCo precursor was obtained by depositing NiCo-hydroxide precursor on CC/BiOI working electrode at a potential of −1.0 V for 300 s in a cell containing 100 mL aqueous solution consisting of $Co(NO_3)_2{\cdot}6H_2O$ (10 mmol) and $Ni(NO_3)_2{\cdot}6H_2O$ (5 mmol)

as the electrolyte, Pt plate as counter electrode, and AgCl electrode as the reference electrode. Next, $NaH_2PO_2{\cdot}H_2O$ (200 mg) was placed in the upstream porcelain boat of a quartz tube of the tubular furnace, while CC/Bi-NiCo precursor was placed in the downstream porcelain boat. The CC/Bi-NCP samples (CC/Bi-NCP-x, where x = 1, 2, and 3 representing 100, 200, and 300 s of electrodeposition time of BiOI, respectively) were obtained by annealing at 300 °C for 2 h under an Ar atmosphere.

By contrast, NiCo hydroxide was directly deposited on the CC and the same phosphating annealing step as that used for CC/Bi-NCP-x was performed to obtain CC/NCP. Digital photographs of the CC/Bi-NCP-2 sample and CC/NCP sample are provided in Figure S33 (Supporting Information).

Characterization: The phase and crystal structure of the samples were analyzed by X-ray diffraction (XRD, D8-Advances, CuKα radiation, λ = 1.5406 Å). The composition of the material was further analyzed by Raman spectroscopy (HORIBA HR800). The morphology of the samples was characterized by scanning electron microscopy (SEM, Hitachi SU8010) and transmission electron microscopy (TEM, JEOL JEM-2200FS). The elemental distribution of the samples was analyzed by energy-dispersive spectroscopy (EDS). The surface chemical state of the material was detected by X-ray photoelectron spectroscopy (XPS, ESCALAB-250, AlKα radiation). The Brunauer–Emmett–Teller (BET) specific surface areas were measured using a micropolitics surface instrument (Micromeritics ASAP 2020Plus) equipped with a porosity analyzer. The surface charges of samples were measured using a Zeta potential analyzer (Mastersizer 2000). The concentrations of elements were determined by inductively coupled plasma-mass spectrometry (ICP-MS, Ultima Expert LT, Horiba, France).

The procedures related to the preparation process of negative electrode materials, preparation process of CC/NCO and CC/Bi-NCO, electrochemical measurement methods, and calculation techniques can be found in Supporting Information.

Statistical Analysis: For material characterization studies including SEM, XRD, XPS, and Raman spectroscopy analyses, the samples were selected randomly from at least three as-synthesized CC/Bi-NCP-2 obtained under the same electrodeposition treatment and annealing conditions. The Jade 9 software was used for the characterization and transformation of XRD data, and the Avantage software was employed to deconvolute and analyze XPS data. During electrochemical analysis, measurements were repeated under the same conditions (25 °C, air atmosphere). All the CV, GCD, and EIS data sets were recorded by using the CHI660e software. The CV curves were normalized based on the corresponding active material mass of the tested cell, and the ZSimpWin software was used to fit the resistances of EIS spectra by using the mentioned model. The ECbox software was employed for fitting the slopes of the calculations of b-value and apparent diffusion coefficient. The remaining measurement data were plotted as recorded. Data were visualized by using Origin 2024 software.

Supporting Information

Supporting Information is available from the Wiley Online Library or from the author.

Acknowledgements

J.X. and X.G. contributed equally to this work. The authors greatly acknowledge the financial support from the Scientific and Technological Development Program of Jilin Province (Grant No. 20240101114JC). The authors are also thankful to the CUPT (China Undergraduate Physics Tournament) Laboratory of the College of Physics at Jilin University for theoretical computing resources.

Conflict of Interest

The authors declare no conflict of interest.

Data Availability Statement

Research data are not shared.

Keywords

bismuth, heterostructure, nickel-cobalt phosphide, supercapacitors

Received: January 27, 2024
Revised: April 16, 2024
Published online: May 17, 2024

[1] C. Choi, D. S. Ashby, D. M. Butts, R. H. DeBlock, Q. Wei, J. Lau, B. Dunn, *Nat. Rev. Mater.* **2020**, *5*, 5.
[2] N. Yang, S. Yu, W. Zhang, H.-M. Cheng, P. Simon, X. Jiang, *Adv. Mater.* **2022**, *34*, 2202380.
[3] S. Balasubramaniam, A. Mohanty, S. K. Balasingam, S. J. Kim, A. Ramadoss, *Nano-Micro Lett.* **2020**, *12*, 85.
[4] L. Bai, Z. Hu, C. Hu, S. Zhang, Y. Ying, Y. Zhang, L. Li, H. Zhang, N. Li, S. Shi, S. Liu, L. Hao, T. Liu, H. Huang, H. Huang, Y. Zhang, *Angew. Chem., Int. Ed.* **2023**, *62*, 202301631.
[5] Z. Liang, C. Qu, W. Zhou, R. Zhao, H. Zhang, B. Zhu, W. Guo, W. Meng, Y. Wu, W. Aftab, Q. Wang, R. Zou, *Adv. Sci.* **2019**, *6*, 1802005.
[6] S. J. Marje, H. B. Tyagaraj, S.-K. Hwang, G. S. Rama Raju, K. S. Ranjith, N. R. Chodankar, Y. S. Huh, Y.-K. Han, *J. Mater. Chem. A* **2023**, *11*, 14586.
[7] M. Li, J. Meng, Q. Li, M. Huang, X. Liu, K. A. Owusu, Z. Liu, L. Mai, *Adv. Funct. Mater.* **2018**, *28*, 1802016.
[8] a) J. Zhao, H. Cheng, Z. Zhang, Y. Liu, J. Song, T. Liu, Y. He, A. Meng, C. Sun, M. Hu, L. Wang, G. Li, J. Huang, Z. Li, *Adv. Funct. Mater.* **2022**, *32*, 2202063; b) K. Li, Z. Guo, Q. Sun, X. Dai, Y. Li, K. Yao, X. Liu, Z. Bao, J. Rao, Y. Zhang, *Chem. Eng. J.* **2023**, *454*, 140223.
[9] Y. Li, J. Cai, J. Zhang, Z. Chen, G. Wang, Q. Chen, M. Chen, *Adv. Energy Mater.* **2023**, *13*, 2204114.
[10] I. Hussain, M. Z. Ansari, M. Ahmad, A. Ali, T. Nawaz, T. Hussain, C. Lamiel, M. Sufyan Javed, X. Chen, M. Sajjad, T. Kaewmaraya, K. Khan, K. Zhang, *Adv. Funct. Mater.* **2023**, *33*, 2302888.
[11] E. Baasanjav, T. G. Senthamaraikannan, P. Bandyopadhyay, D.-H. Lim, S. M. Jeong, *Chem. Eng. J.* **2023**, *466*, 143064.
[12] R. Li, Y. Li, P. Yang, D. Wang, H. Xu, B. Wang, F. Meng, J. Zhang, M. An, *J. Energy Chem.* **2021**, *57*, 547.
[13] H. Lv, Q. Pan, Y. Song, X.-X. Liu, T. Liu, *Nano-Micro Lett.* **2020**, *12*, 118.
[14] X. Liu, W. Xu, D. Zheng, Z. Li, Y. Zeng, X. Lu, *J. Mater. Chem. A* **2020**, *8*, 17938.
[15] X. Sun, Z. Meng, Z. Hao, Z. Du, J. Xu, H. Nan, W. Shi, F. Zeng, X. Hu, H. Tian, *J. Colloid Interface Sci.* **2023**, *630*, 618.
[16] a) Z.-H. Huang, Y. Song, D.-Y. Feng, Z. Sun, X. Sun, X.-X. Liu, *ACS Nano* **2018**, *12*, 3557; b) H. Li, S. Lin, H. Li, Z. Wu, Q. Chen, L. Zhu, C. Li, X. Zhu, Y. Sun, *Small Methods* **2022**, *6*, 2101320.
[17] Y. Chen, Z. Yin, D. Huang, L. Lei, S. Chen, M. Yan, L. Du, R. Xiao, M. Cheng, *J. Colloid Interface Sci.* **2022**, *611*, 356.
[18] Y. Shi, M. Zhang, J. Zhao, L. Zhang, X. Cui, X. Zhu, J. Su, D. Yang, J. Li, *J. Electrochem. Soc.* **2021**, *168*, 122502.
[19] H. Qian, Y. Liu, H. Chen, K. Feng, K. Jia, K. Pan, G. Wang, T. Huang, X. Pang, Q. Zhang, *Energy Storage Mater.* **2023**, *58*, 232.
[20] a) P. Subramanyam, B. Meena, D. Suryakala, M. Deepa, C. Subrahmanyam, *Catal. Today* **2021**, *379*, 1; b) Y. Li, K. Lv, W. Ho, Z. Zhao, Y. Huang, *Chin. J. Catal.* **2017**, *38*, 321.
[21] T. Qin, D. Wang, X. Zhang, Y. Wang, N. E. Drewett, W. Zhang, T. Dong, T. Li, Z. Wang, T. Deng, Z. Pan, N. Yue, R. Yang, K. Huang, S. Feng, R. Huang, W. Zheng, *Energy Storage Mater.* **2021**, *36*, 376.

[22] Y. Wang, J. Luo, L. Zhou, X. Lu, *J. Power Sources* **2022**, *544*, 231903.
[23] A. D. Jagadale, V. S. Kumbhar, R. N. Bulakhe, C. D. Lokhande, *Energy* **2014**, *64*, 234.
[24] L. Pu, K. Li, Z. Chen, P. Zhang, X. Zhang, Z. Fu, *J. Power Sources* **2014**, *268*, 476.
[25] Y. Yuan, G. Luo, N. Li, *RSC Adv.* **2021**, *11*, 31526.
[26] S. J. Marje, S. S. Pujari, S. A. Khalate, V. V. Patil, V. G. Parale, T. Kim, H.-H. Park, J. L. Gunjakar, C. D. Lokhande, U. M. Patil, *J. Mater. Chem. A* **2022**, *10*, 11225.
[27] B. Scharifker, G. Hills, *Electrochim. Acta* **1983**, *28*, 879.
[28] P. Liu, X. Zhang, L. Feng, H. Pan, B. Yang, X. Zheng, G. Dong, *J. Mater. Chem. A* **2021**, *9*, 15472.
[29] Z. Yan, H. Sun, X. Chen, H. Liu, Y. Zhao, H. Li, W. Xie, F. Cheng, J. Chen, *Nat. Commun.* **2018**, *9*, 2373.
[30] a) W. Song, J. Wu, G. Wang, S. Tang, G. Chen, M. Cui, X. Meng, *Adv. Funct. Mater.* **2018**, *28*, 1804620; b) H. C. Chen, S. Jiang, B. Xu, C. Huang, Y. Hu, Y. Qin, M. He, H. Cao, *J. Mater. Chem. A* **2019**, *7*, 6241; c) Y. Lin, K. Sun, S. Liu, X. Chen, Y. Cheng, W.-C. Cheong, Z. Chen, L. Zheng, J. Zhang, X. Li, Y. Pan, C. Chen, *Adv. Energy Mater.* **2019**, *9*, 1901213.
[31] R. Hu, L. Jiao, H. Liang, Z. Feng, B. Gao, X.-F. Wang, X.-Z. Song, L.-Z. Liu, Z. Tan, *Small* **2023**, *19*, 2304132.
[32] a) H. Liang, C. Xia, Q. Jiang, A. N. Gandi, U. Schwingenschlögl, H. N. Alshareef, *Nano Energy* **2017**, *35*, 331; b) T. Wang, X. Liu, Z. Yan, Y. Teng, R. Li, J. Zhang, T. Peng, *ACS Sustainable Chem. Eng.* **2019**, *8*, 1240; c) R. Ding, X. Li, W. Shi, Q. Xu, E. Liu, *Chem. Eng. J.* **2017**, *320*, 376.
[33] a) G. Zhang, Y. Li, R. Zhu, Z. Huang, D. Zhang, Z. Long, Y. Li, *Small* **2024**, *20* , 2305136; b) C. Yang, P. Wang, Z. Xiong, X. Wu, H. Chen, J. Xiao, G. Zhou, L. Liang, G. Hou, D. Li, J. Z. Liu, H.-M. Cheng, L. Qiu, *Energy Storage Mater.* **2023**, *60*, 102843; c) T. Zhai, L. Wan, S. Sun, Q. Chen, J. Sun, Q. Xia, H. Xia, *Adv. Mater.* **2017**, *29*, 1604167; d) X. Gao, Y. Zhang, Y. Zhao, S. Yin, J. Gui, C. Sun, S. Guo, *Nano Energy* **2022**, *91*, 106701.
[34] a) Z. Fang, L. Peng, Y. Qian, X. Zhang, Y. Xie, J. J. Cha, G. Yu, *J. Am. Chem. Soc.* **2018**, *140*, 5241; b) H. Wang, C. Li, J. An, Y. Zhuang, S. Tao, *J. Mater. Chem. A* **2021**, *9*, 18421.
[35] Z. Lu, Z. Hu, L. Xiao, Y. Xie, N. Li, L. Xi, W. Chen, J. Xiao, Y. Zhu, *Chem. Eng. J.* **2022**, *450*, 138347.
[36] a) J. Wang, W. Guo, Z. Liu, Q. Zhang, *Adv. Energy Mater.* **2023**, *13*, 2300224; b) A. M. Patil, S. Moon, A. A. Jadhav, J. Hong, K. Kang, S. C. Jun, *Adv. Funct. Mater.* **2023**, *33*, 2305264.
[37] C. Zhang, Y. Cui, Y. Yang, L. Lu, S. Yu, Z. Meng, Y. Wu, Y. Li, Y. Wang, H. Tian, W. Zheng, *Adv. Funct. Mater.* **2021**, *31*, 2105372.
[38] C. Li, X. Wang, D. Ma, Y. Yan, P. Huo, Q. Yang, *Adv. Sci.* **2023**, *10*, 2301398.
[39] Q. Liu, J. Huang, H. Tang, X. Yu, J. Shen, *J. Mater. Sci. Technol.* **2020**, *56*, 196.
[40] L. Xu, C. Huang, Z. Hua, L. Chen, *Energy Storage Mater.* **2023**, *61*, 102888.
[41] a) X. Gao, L. Yin, L. Zhang, Y. Zhao, B. Zhang, *Chem. Eng. J.* **2020**, *395*, 125058; b) X. Shan, Z. Guo, Z. Qu, Y. Zou, L. Zhao, P. Chen, *Mater. Res. Lett.* **2022**, *10*, 593.
[42] a) J. Johnson William, I. Manohara Babu, G. Muralidharan, *Chem. Eng. J.* **2021**, *422*, 130058; b) G. Zan, T. Wu, P. Hu, Y. Zhou, S. Zhao, S. Xu, J. Chen, Y. Cui, Q. Wu, *Energy Storage Mater.* **2020**, *28*, 82; c) Y. L. Liu, M. Q. Li, G. G. Wang, L. Y. Dang, F. Li, M. E. Pam, H.-Y. Zhang, J.-C. Han, H. Y. Yang, *ENERGY ENVIRON. MATER.* **2021**, *4*, 465; d) P. A. Shinde, A. G. Olabi, N. R. Chodankar, S. J. Patil, S.-K. Hwang, M. A. Abdelkareem, *Chem. Eng. J.* **2023**, *454*, 140246; e) J. Song, T. Liu, Y. He, Y. Wang, Y. Zhang, A. Meng, X. Yuan, L. Wang, G. Li, J. Zhao, Z. Li, *Sci. China Mater.* **2023**, *66*, 1767.
[43] a) Z. Peng, C. Yang, Q. Zhao, F. Liang, S. Yun, R. Liu, Z. Zhang, Y. Liao, H. C. Chen, *J. Colloid Interface Sci.* **2022**, *607*, 61; b) J. Li, Y. Ding, S. Zhang, H. Li, B. Yin, T. Ma, *J. Power Sources* **2022**, *524*, 231074; c) S. Yang, H. Lv, Y. Wang, X. Guo, L. Zhao, H. Li, C. Zhi, *Angew. Chem., Int. Ed.* **2022**, *61*, e202209794; d) R. Liu, J. Huang, Y. Diao, W. Zhao, H.-C. Chen, *J. Colloid Interface Sci.* **2023**, *639*, 263.
[44] K. J. McDonald, K. S. Choi, *Energy Environ. Sci.* **2012**, *5*, 8553.